Materials & Design 220 (2022) 110836

Contents lists available at ScienceDirect

Materials & Design

journal homepage: www.elsevier.com/locate/matdes

Dynamic cryo-mechanical properties of additively manufactured nanocrystalline nickel 3D microarchitectures

Jakob Schwiedrzik [a,*,1], Rajaprakash Ramachandramoorthy [a,b,*,1], Thomas E.J. Edwards [a], Patrik Schürch [a], Daniele Casari [a], Maria J. Duarte [b], Gaurav Mohanty [c], Gerhard Dehm [b], Xavier Maeder [a], Laetitia Philippe [a], Jean-Marc Breguet [d], Johann Michler [a]

[a] Empa Swiss Federal Laboratories for Materials Science and Engineering, Laboratory for Mechanics of Materials and Nanostructures, Feuerwerkerstrasse 39, 3602 Thun, Switzerland
[b] Max-Planck-Institut für Eisenforschung GmbH, Structures and Micro/Nano Mechanics Department, Max-Planck-Strasse 1, 40237 Düsseldorf, Germany
[c] Materials Science and Environmental Engineering, Faculty of Engineering and Natural Sciences, Tampere University, 33014 Tampere, Finland
[d] Alemnis AG, Schorenstrasse 39, 3645 Thun, Switzerland

HIGHLIGHTS

- Metal micropillars were synthesized by template-assisted electrodeposition.
- Mechanical testing was performed at cryogenic temperatures and high strain rates.
- Structure-property relationships were identified for a large range of conditions.
- The deformation mechanism was identified to be collective dislocation nucleation.
- 3D Microlattices showcase the promise of the method for complex microarchitectures.

GRAPHICAL ABSTRACT

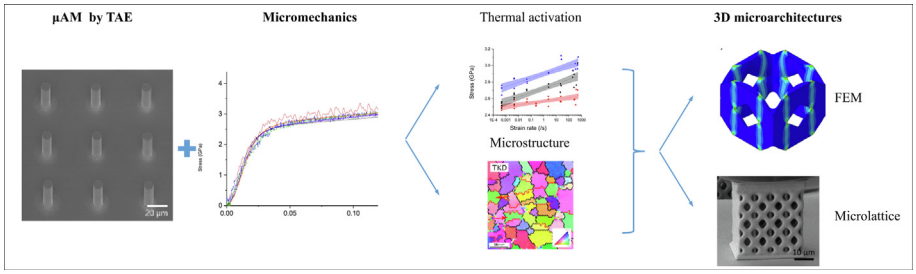

ARTICLE INFO

Article history:
Received 11 March 2022
Revised 3 June 2022
Accepted 4 June 2022
Available online 10 June 2022

Keywords:
Nanocrystalline nickel
Micromechanics
Cryogenic temperature
High strain rate
Microlattices

ABSTRACT

Template-assisted electrodeposition is a promising microscale additive manufacturing technique allowing to deposit pure metals with high resolution. To allow the application-relevant design of metamaterials, it is necessary to establish microstructure-mechanical property relationships under extreme conditions. In this work, a novel process based on two-photon lithography was used to synthesize arrays of nanocrystalline nickel micropillars and complex microlattices. This allowed high throughput mechanical testing using a newly developed *in situ* nanoindenter at unprecedented combination of cryogenic temperatures (160 to 300 K) and strain rates (0.001 to 500 s^{-1}). Strain rate sensitivity was found to increase from ~ 0.004 at 300 K to ~ 0.008 at 160 K. Thermal activation analysis showed a decrease in activation volume from $122b^3$ at 300 K to $45b^3$ at 160 K and an activation energy of 0.59 eV in line with collective dislocation nucleation as the rate limiting mechanism. Transmission Kikuchi Diffraction allowed quantifying microstructural changes during deformation. As such, a deformation map along with the responsible deformation mechanisms has been ascertained for additively micromanufactured

Abbreviations: MEMS, Micro electro-mechanical system; TAE, Template-assisted electrodeposition; FIB, Focused ion beam; APT, Atom probe tomography; TKD, Transmission Kikuchi diffraction; XRD, X-ray diffraction; FEM, Finite element method; SEM, Scanning electron microscope; TEM, Transmission electron microscope; EBSD, Electron backscatter diffraction; HAGB, High angle grain boundary; LAGB, Low angle grain boundary; TB, Twin boundary; PDMP, Partial dislocation mediated process; SFE, Stacking fault energy; CTB, Coherent twin boundary; KUBC, Kinematic uniform boundary condition.

* Corresponding authors at: Empa, Feuerwerkerstrasse 39, CH-3602 Thun, Switzerland (J. Schwiedrzik) and MPIE, Max-Planck-Strasse 1, 40237 Düsseldorf, Germany (R. Ramachandramoorthy).
E-mail addresses: jakob.schwiedrzik@empa.ch (J. Schwiedrzik), r.ram@mpie.de (R. Ramachandramoorthy).
[1] Equal Contribution.

https://doi.org/10.1016/j.matdes.2022.110836

nanocrystalline nickel at unique combinations of extreme temperatures and strain rates. Further, rate-dependent compression of microlattices and complementary finite element simulations using the results from micropillars as constitutive models exemplified the promise of such metal microarchitectures in space and aviation applications.

1. Introduction

The synthesis and characterization of nanocrystalline metals, with grain size <100 nm, has been a topic of intense research in the material science community, given the push for creating ultra-strong metals via microstructure engineering. They find wide applications in microcomponents, micro electro-mechanical system (MEMS), and other small-scale structures. The ability to fabricate nanocrystalline structures at small scales will open up a host of new applications including precision watchmaking and impact protection of sensitive microsensors.

Template-assisted electrodeposition (TAE) is a electrochemical additive manufacturing technique that allows the creation of metallic structures at micrometer length scales. A non-conductive template is created on a conductive substrate and subsequently metal is electrodeposited into it. Removal of the template (and substrate) yields free-standing metallic microcomponents. Nickel is one of the most prominent elements to be electrodeposited, due to its use as hard coating, corrosion protection, decorative surface finish, and low internal stress [1]. In TAE, electrodeposition can be combined with any lithography technique allowing high throughput synthesis of microscale structures at ambient temperature. The first 2D microcomponents were synthesized by Becker and Ehrfeld in 1981 with X-ray lithography [2], e-beam and UV-lithography followed shortly after. 3D microarchitectures have been recently prepared using colloidal templates, stereo- and two-photon lithography [3,4]. Two-photon lithography is a novel technique allowing the creation of free-form complex 3D templates with sub-micron resolution [5]. In the past, various structures have been created such as gold helices [6], copper lattices [7] and nickel 3D structures [8–10]. The microstructure of the deposit is dominated by low angle grain boundaries (LAGB) [11] and often features a texture, leading to mechanical anisotropy [12].

A method for directly measuring microscale yield properties and post-yield behavior is micropillar compression [13]. Pillars of μm size are usually milled on the surface of a sample using a focused ion beam (FIB) and subsequently compressed using a nanoindenter equipped with a flat punch recording force and tip displacement simultaneously. Due to the homogeneous, uniaxial loading conditions [14], the setup allows a straight forward interpretation in terms of stress–strain behavior. This allows measuring compressive properties at the microscale in a quantitative fashion for all classes of materials [15–19]. Nanocrystalline metals have been previously tested with pillars fabricated using FIB-based milling [20–22]. Unfortunately, the use of FIB often results in artificial grain growth and the formation of a thin damaged layer at the surface that affects the measured properties [23]. Therefore, TAE offers an attractive alternative for measuring the mechanical properties of pristine microstructures.

The measurement of mechanical properties as a function of temperature and strain rate is of particular interest, as it allows calculating thermal activation parameters and identifying the nature of the dominating rate-limiting deformation mechanisms [24,25]. Such experiments have been performed using various micromechanical techniques on different materials like ceramics, metals, and semiconductors [26–28]. Especially for materials with a metastable microstructure like nanocrystalline metals, it is important that the microstructure is not altered by the temperature profile employed for thermal activation analysis. In this context, experiments at sub-ambient temperatures may be used to minimize temperature induced changes in grain structure.

The mechanical properties of ncNi have been studied extensively in the past. Studies on ncNi with macroscopic sample dimensions have identified a low strain rate sensitivity (∼0.007–0.03) in the strain rate range of 0.0001/s to 1000/s and grain-boundary mediated dislocation activities as the primary deformation mechanism [29–33]. It should be noted that macroscale experiments are typically conducted only between strain rates of 0.001/s and 0.1/s (using universal testing systems) and at strain rates of 1000/s and higher (using Kolsky bars and split Hopkinson pressure bars) [34]. This leaves a knowledge gap between 0.1/s and 1000/s, which can now be addressed due to the recent development of high strain rate micromechanical testing [34]. Beyond 1000/s, a steep increase in SRS for ncNi under compression was reported [32] due to dislocation pile-up within the grain interior and shear banding with local grain growth. Several studies have measured thermomechanical properties of ncNi at the macroscale, e.g. cryogenic tensile properties at quasi-static speeds [1,35–37] as well as at elevated temperatures [38,39]. Recently, using nanoindentation and micropillar compression, the properties of ncNi have also been identified at room and elevated temperature conditions [20,21,34,40–42]. What is currently missing is an investigation of the strain rate dependent properties of ncNi under cryogenic conditions and in a large range of strain rates using a statistically relevant number of microscale specimens.

From an application perspective, it is imperative to fabricate and analyze complex architectures such as microlattices, which are specifically designed to possess a combination of desirable properties like high specific strength and ductility. Metallic metamaterials are especially attractive, as they allow to reach higher specific strengths through the intentional use of well-known intrinsic and extrinsic size effects [43]. Extrinsic size effects are dictated by the external dimensions of the structural components making up the metamaterial [44]. Work has been conducted on identifying optimized structures and the dependence of their apparent properties on strut size [45]. The intrinsic size effect is controlled by the microstructure of the metal. Specifically, grain size, type of grain boundary, and texture are responsible for the apparent mechanical properties [46]. Combining intrinsic and extrinsic size effects allows to leverage the mechanical properties and populate uncharted regions in the material property space.

The goal of this study was to identify the mechanical behavior of ncNi micropillars as a baseline for the future design of metallic metamaterials. Large arrays of micropillars were fabricated by TAE. Their microstructure was analyzed using Atom Probe Tomography (APT), Transmission Kikuchi Diffraction (TKD), as well as X-ray Diffraction (XRD) and rationalized by simulations of the electrodeposition process. Micropillar compression experiments were performed at subambient temperatures (160 K to 300 K) and in a wide range of strain rates (0.001 to 500/s) to determine strain rate sensitivity and thermal activation parameters. In addition, high-

resolution Scanning Electron Microscopy (HR-SEM) images and TKD analysis on deformed micropillars allowed assessing the microstructural changes induced by the deformation at varying loading conditions. Further, ncNi microlattices were fabricated and subsequently tested in compression at strain rates from 0.0006/s to 0.06/s. The observed stress–strain behavior and failure mode were compared to finite element simulations of the microlattice unit cell to obtain further insights into the deformation behavior of these complex metallic microarchitectures.

2. Experimental

2.1. Template-assisted electrodeposition

Micropillars with a diameter of 3.5 μm and a height of 10 μm and microlattices with dimensions 33 × 33 × 30 μm^3 were fabricated using the following process: ITO-coated cover glass slides (Thermofischer #1) were cleaned with 150 W oxygen plasma for 300 s and used as substrates. The samples were afterward heated at 160 °C for 300 s to desorb water molecules from the surface. AZ9260 photoresist was spin coated onto the cleaned glass slides. The photoresist was drop cast and spun at 500 rpm for 5 s and 1600 rpm for 60 s. The samples were then let to rest for 60 s before hot-baking at 90 °C for 60 s and 140 s at 110 °C. The samples were let rehydrate for 3600 s. The rehydrated samples were then patterned with a two photon lithography 3D printer (Professional GT, Nanoscribe, Germany). The structure array was illuminated and samples developed immediately after illumination. The development was carried out in AK400/de-ionized water (18 M mixture in ratio 1:5). The duration of the development was 360 s with a subsequent wash in de-ionized water for 600 s. The samples were then air-dried.

For electrodeposition, the nickel electrolyte was mixed with deionized water. The electrolyte contained 1.19 M nickel sulfamate, 0.3 M nickel chloride, 0.75 M boric acid, 0.0109 M saccharine, and 0.04 mM sodium dodecyl sulfate. The electrodeposition was performed in a 500 ml electrochemical glass cell with a nickel counter anode and Ag/AgCl reference electrode, using the template as a working electrode. The bath was heated to 50 °C. No artificial convection was used. The deposition was carried out for 5400 s at a deposition potential of −1.2 V vs Ag/AgCl. The samples were removed from the electrochemical cell and mounted onto a copper SEM stub using a thermally conductive epoxy adhesive (Stycast 2850 FT, Henkel, Germany). After the epoxy was hardened, the samples were submerged into acetone and sonicated for 5 s to allow removing the ITO glass slide. The samples were cleaned in acetone and isopropanol. A schematic overview of the synthesis process is shown in Fig. 1.

2.2. Simulation of the electrodeposition process

A two-dimensional, time-dependent tertiary current distribution simulation of the electrodeposition process based on the finite element method (FEM) was performed using the electrodeposition module of COMSOL Multiphysics 5.3 (Comsol Inc., Sweden). The set of equations used in this work is based on prior studies [8,9]. The ion flux was calculated based on the Nernst-Planck equation, a mass and current balance equation, and the electrode growth velocity equation based on the local current, which was calculated by the Butler-Volmer equation. The ion mobility was derived through the Nernst-Einstein relation. To account for the supporting electrolyte, the conductivity was measured and added to the model. The bulk electrolyte region was meshed coarsely, while the micropillar template was meshed finely to ensure high precision and fidelity of the results. The meshing of the pillars was refined to the point where a further decrease of the mesh size did not influence the result. The used modeling parameters can be found in a prior study [9].

2.3. Extreme micromechanical testing instrumentation

An *in situ* microindenter (Alemnis AG, Switzerland) for use inside an SEM was modified for use at sub-ambient temperatures and quasistatic strain rates (Fig. 2a). During operation, liquid nitrogen is stored in a 25 l dewar outside the vacuum chamber, evaporated on a fine copper grid and pumped through a cold finger attached to the back of the indenter frame with isolating shafts. The cold finger is linked to the sample and tip holders using copper braids to reach a stable baseline temperature. The frame and electronic components are isolated from the cooled region by ceramic shafts. The noise floor of the low temperature indenter is approximately 1 nm RMS in displacement and 12 μN RMS in force at 20 Hz sampling rate during the operation of both nitrogen and vacuum pumps. Frame drift is minimized by holding the frame temperature constant using resistive heaters and temperature feedback in a closed loop control. Furthermore, thermal sensors and resistive heaters are attached to both sample and tip holders to allow local temperature sensing and tuning. The frame compliance was determined by continuous stiffness measurements on a Cu sample using a Berkovich tip at room temperature to be 4.85 nm/mN.

For performing experiments at subambient temperatures and high strain rates, the cryogenic *in situ* micromechanical instrument was further modified (Fig. 2b). The load cell was replaced by a high stiffness piezoelectric load sensor and the tip side cooling was removed to prevent temperature-dependent piezoelectric interference with load sensing. The high strain rate instrument features a piezoelectric actuator that is powered using a high voltage amplifier capable of outputting high voltages (±175 V) with very high slew rates (350 V/μs) allowing a maximum tip displacement rate of 8 mm/s. The voltage output of the piezoelectric load cell is amplified by a high impedance amplifier. The displacement and load signals at high strain rates are captured using a digital data acquisition system at up to 1 MHz. The noise floor of this system is approximately 13 nm RMS in displacement and 0.5 mN in force at the maximum sampling rate. The frame compliance was determined by indentations in a reference fused silica sample to be approximately 0.7 nm/mN.

2.4. Mechanical experiments and data analysis

Micropillars were compressed monotonically inside an SEM (Zeiss DSM 962, Germany). Experiments were performed in displacement control using the instruments described above equipped with a flat punch diamond indenter (diameter 10 μm). Mechanical testing was performed at 160 K, 224 K, and 300 K, and at strain rates ranging from 10^{-3} to 500/s. Load and displacement were measured simultaneously. The load–displacement data were subsequently converted to engineering stress–strain data, using the top cross-sectional area and height of the micropillar, respectively. The yield stress was extracted using a 2% strain offset criterion to ensure consistency of the results despite varying noise levels for the different strain rates.

Based on this dataset, apparent activation volume was calculated using Eq. (1) [24]:

$$V_{app} = \sqrt{3} k_B T \left(\frac{d \ln \dot{\varepsilon}}{d\sigma}\right) \quad (1)$$

with a length of 1.473 nm for the Burgers vector b of partial dislocations in nickel [47], the Boltzmann constant k_B, and temperature T. Given the previous theoretical and experimental evidence that the deformation process in nanocrystalline nickel most likely

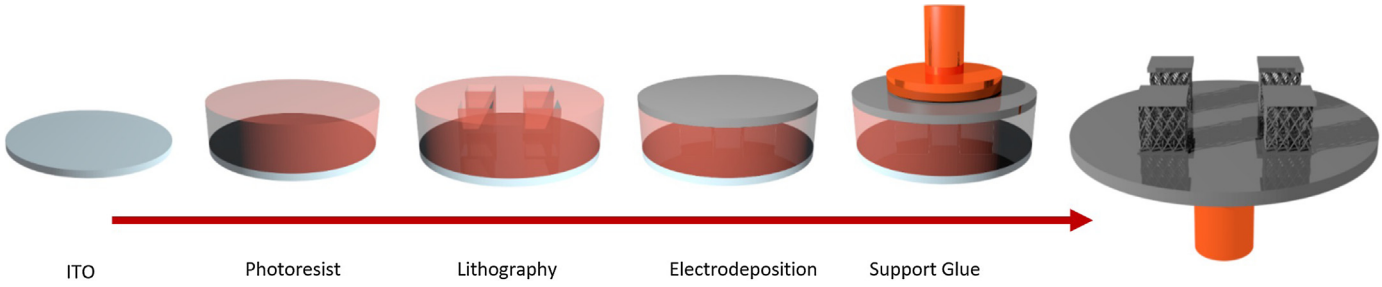

Fig. 1. Schematical overview of the template-assisted electrodeposition process used for fabricating ncNi micropillars and microlattices.

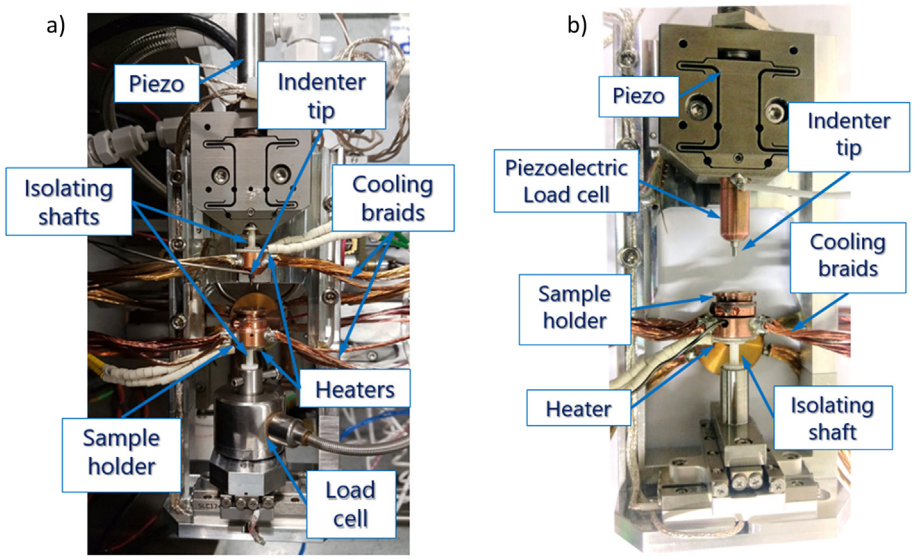

Fig. 2. a) In situ indenter customized for quasistatic experiments at subambient temperatures. b) Modified version of the *in situ* indenter capable of performing high strain rate experiments at subambient temperatures.

proceeds via emission of partial dislocations, the corresponding appropriate burgers vector has been chosen for the activation volume calculation [47–49]. For determining apparent activation energy, strain rates were extrapolated from linear regressions of yield stress vs. strain rate for a stress level of 2.65 GPa. Then, the natural logarithm of the extrapolated strain rates was plotted over 1/T and the activation energy was determined as the slope of the linear fit to the data points [21].

2.5. Material analytics

Images of pristine and deformed micropillars were taken using a high-resolution scanning electron microscope (HRSEM, Hitachi S4800, Japan) at an acceleration voltage of 3 kV.

X-ray diffraction measurements were performed on a Discover D8 diffractometer (Bruker, Germany) using a Cu-Kα source with 40 kV and 40 nA, with a coupled 2θ-θ Bragg-Brentano configuration, using a step size of 0.02°. The average grain size was determined using the Scherrer equation [50] on the (1 1 1) peak of the nanocrystalline nickel diffractograms.

Thin lamellae of the micropillars for further analysis requiring electron transparency were obtained by a focused ion beam lift out process with preliminary protection by electron beam-assisted platinum (Pt) deposition from a metal–organic precursor gas, followed by ion-beam assisted Pt deposition. Transmission electron microscopy (TEM) imaging was performed on a JEM2200fs (Jeol, Japan) in both bright field projection (BF-TEM) and high resolution (HR-TEM) modes. Transmission Kikuchi diffraction was performed on the same thin lamellae to generate quantified grain and texture statistics, using an electron backscatter diffraction (EBSD) detector (DigiView 5, TSL/EDAX, USA) mounted on a scanning electron microscope (Mira, Tescan, Czech Republic) operated at 30 kV, 10nA. TKD scans were operated with a 5 nm step hexagonal raster across three 600 $\times$ 600 nm^2 regions per material condition, each containing over 100 grains which were identified with a 5° misorientation tolerance criterion following an initial single-step grain dilation procedure with a cut-off grain size of 5 pixels. TKD data analysis was performed using the OIM Analytics software (TSL/EDAX, USA).

The specimens for atom probe tomography (APT) were prepared by FIB, using a dual beam workstation (FEI Helios 600i). Individual pillars were lifted out and mounted on standard Si posts for APT, followed by annular milling for tip sharpening at 30 kV. A final tip cleaning was performed at 3 kV and 47 pA to minimize the Ga content. The conditions for the APT measurements (LEAP 5000 XR) were set in voltage mode at a base temperature of 70 K, 200 kHz pulse repetition rate with a 15% target pulse fraction for evaporation and finally a detection rate of 0.005 atoms per pulse. The reconstructions were analyzed using the software IVAS 3.8.2. The data presented in this paper correspond to the evaluation of three APT runs.

2.6. Finite element simulations of the mechanical behaviour of microlattices

FEM simulations were performed using the commercial implicit solver Abaqus/Standard (Dassault Systemes, France). An idealized unit cell of the microlattice structure with a side length of 8 μm

and a range of elliptical strut cross sections (a = 2.7 to 3.3 μm, b = 1.35 to 1.65 μm) measured by HRSEM was considered. Kinematic uniform boundary conditions were applied to the side faces of the unit cell constraining movement in the direction of their respective normal vectors. A uniaxial compression was simulated by adding two rigid surfaces at the top and bottom of the unit cell, implementing hard, frictionless contact conditions, fixing the bottom surface, and displacing the top surface downward by 0.96 μm. A von Mises plasticity model was used with strain rate dependent yield properties extracted from the experimental dataset obtained in this study. The unit cell was meshed with approximately 110,000 quadratic tetrahedral elements (C3D10). The resultant force on the top surface was converted to engineering stress by dividing it by the initial cross sectional area of the unit cell. Engineering strain was calculated by dividing the top surface displacement by the initial height of the unit cell.

3. Results

A novel process based on template assisted electrodeposition (Fig. 1) was developed and used to synthesize large arrays of ncNi micropillars (Fig. 3a left), which were found to be highly reproducible (Fig. 3a right). XRD analysis of the electrodeposited specimen showed no clear texture and an average grain size of ~ 30 nm (Fig. 3c). On the other hand, transmission electron microscopy (Fig. 3b) and TKD analysis of FIB lift-out lamellae from undeformed micropillars (Fig. 7a) revealed a columnar grain structure consisting of elongated grains with an aspect ratio of approximately 2:1. The smallest grain dimension was found to be approximately 30 nm from TKD measurements in line with XRD data.

Finite element simulations of the electrodeposition process enabled the investigation of possible changes in ncNi microstructure arising due to confined electrodeposition within the molds (Fig. 3d). An increase in current density by ~ 1% (<1 mA/cm^2) was found while filling up the molds in comparison to the free growth of the bulk substrate.

APT measurements of the electrodeposited nickel micropillars allowed assessing the composition and spatial distribution of elements within the pillar microstructure. Pillars were shown to contain approximately 99.68 at.% nickel as well as impurities, mainly sulphur/oxygen, carbon and copper in about 0.10 (±0.02) at.% in each case, and in lower concentrations also nitrogen and iron < 0.02 at.%. Sulphur and oxygen contributions cannot be separated since they overlap in the mass spectrum. These impurities mostly segregate towards the grain boundaries, as shown in Fig. 4a) and b). The grain size of ~ 30 nm in line with TKD and XRD is highlighted by the impurity segregation in the corresponding density plot. It should be noted that the impurity segregation is inhomogeneous and consequently the impurities content varies from 0 to 1.5 at.% for different grain boundaries.

Representative engineering stress–strain curves of micropillar compression experiments performed at subambient temperatures (160 K, 224 K, and 300 K) and 6 different strain rates (10^{-3} to 500/s) are shown in Fig. 5a and b. After the initial linear elastic region, micropillars yield between 2.5 and 3 GPa and deform with little apparent strain hardening. Assuming isovolumetric deformation, the engineering stress–strain curves were also converted to true stress–strain curves and it was confirmed that no apparent strain hardening was noticed at any strain rate or temperature (Supplementary Fig. 1). No load serrations were observed for any tested temperature and strain rate. Strain rate sensitivity m was found to be very low with m = 0.0036 at room temperature (Fig. 5c) and slightly increased at subambient temperatures of 240 K and 160 K (m = 0.0085 and 0.0077, respectively). This was

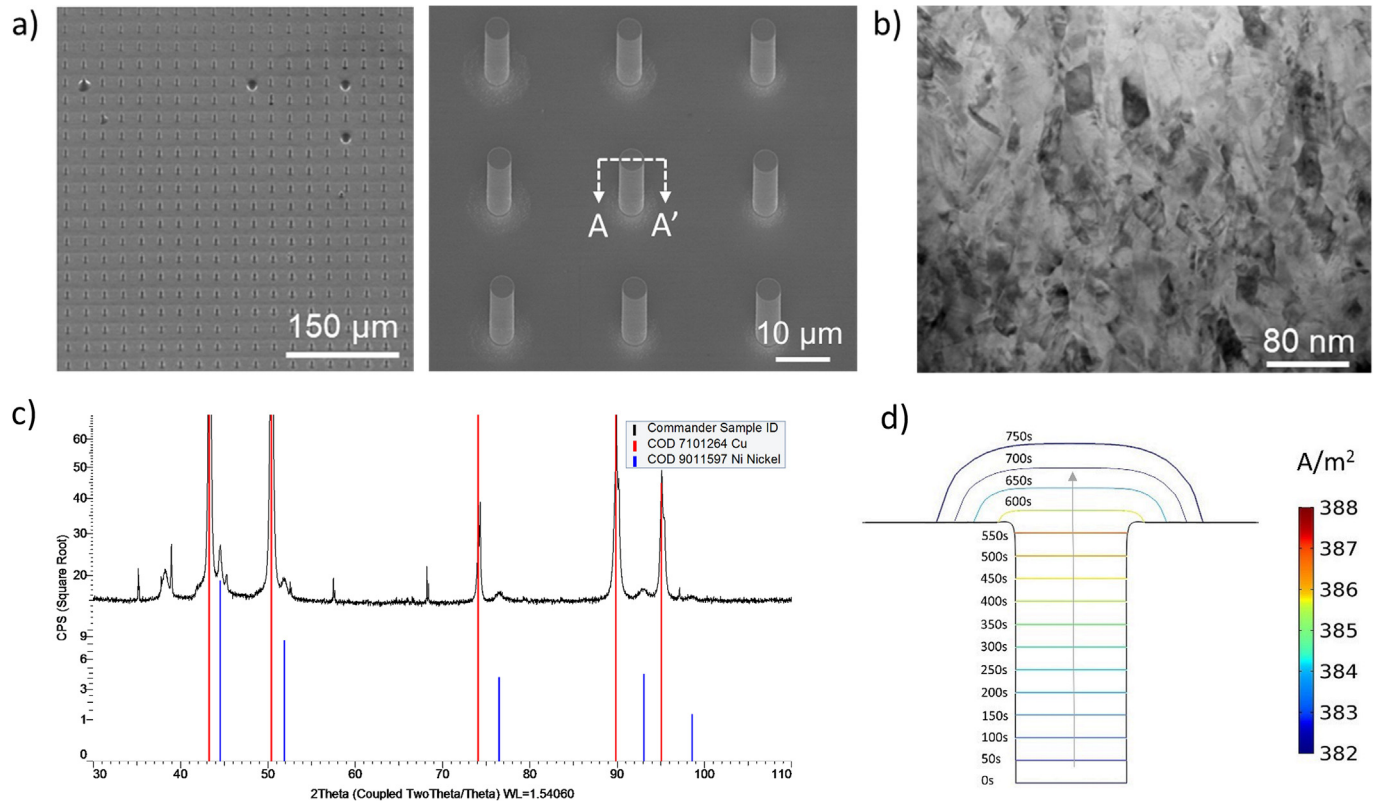

Fig. 3. a) Overview of the micropillar array prepared by template-assisted electrodeposition of nickel. Right. Zoomed in view of electrodeposited nickel micropillars. b) Bright field TEM image of the undeformed nickel microstructure along the vertical direction (A-A' pillar cross-section shown in a)). c) XRD spectrum of the nanocrystalline nickel sample. d) Current density profiles at the deposit surface as a function of deposition time simulated using COMSOL.

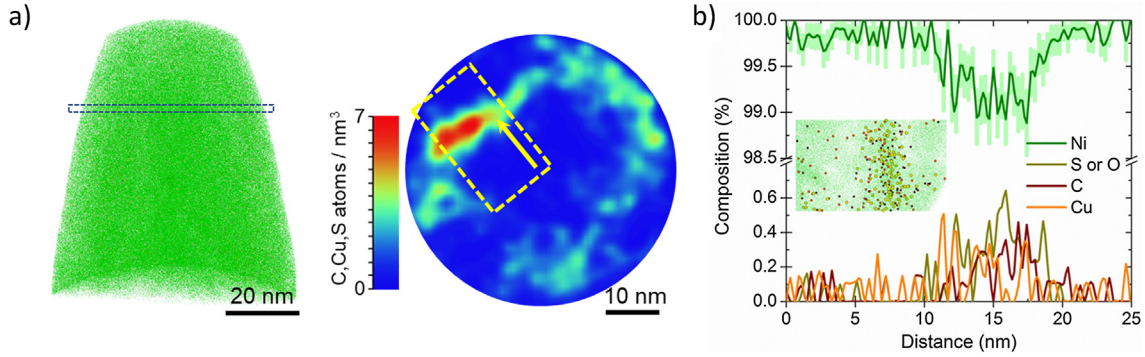

Fig. 4. a) APT reconstruction of a nickel micropillar, along with 2D density plot of the main impurities in a 5 nm virtual cross-section, signaled with dashed lines in the reconstruction. b) Concentration profile along the region highlighted with yellow dashed lines in the density plot.

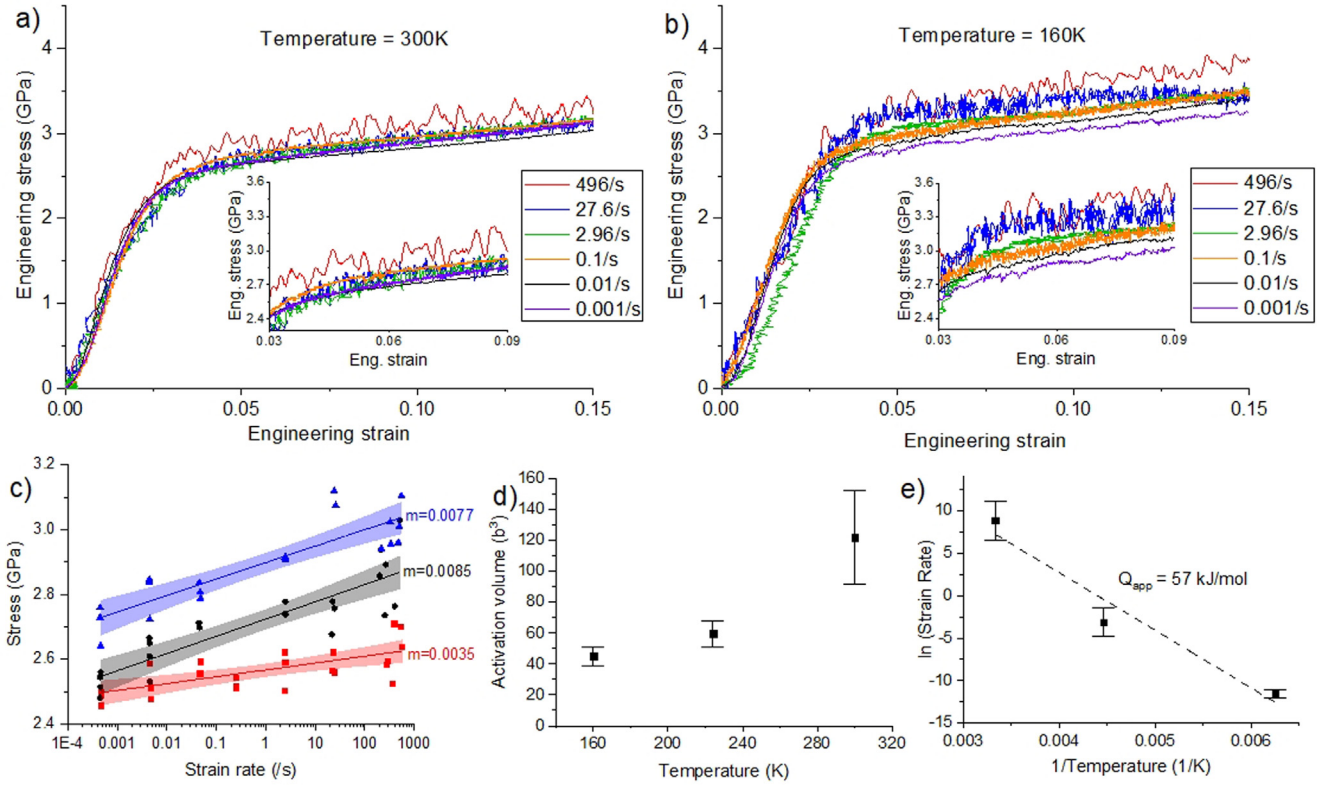

Fig. 5. Engineering stress–strain curves of micropillar compression experiments at a) 300 K and b) 160 K at varying strain rates. c) Extracted micropillar yield stress vs. applied strain rate as a function of temperature. Blue triangles represent data measured at 160 K, black circles at 224 K and red squares at 300 K. d) Activation volume (b^3) as a function of temperature and e) Plot of $\ln(\dot{\varepsilon})$ versus 1/T and extracted apparent activation energy Q_{app}. Error bars in d) and e) were calculated based on error propagation of the standard error of the estimate of the coefficients from the regression analyses.

verified statistically by analysis of covariance (ANCOVA) [51], which showed significant differences ($p < 0.05$) between the slopes of linear regressions between the logarithms of yield stress and strain rate at room temperature and subambient temperatures, respectively.

To investigate the nature of the thermally activated deformation process in further detail, apparent activation volume and energy were determined. V_{app} was found to decrease with decreasing temperature from approximately $122b^3$ at 300 K (similar to previous room temperature studies [21,37]) to $59b^3$ at 240 K and $45b^3$ at 160 K (Fig. 5d). The apparent activation energy was found to be 57 kJ/mol or 0.59 eV (Fig. 5e).

High resolution SEM images of deformed specimens (Fig. 6) revealed homogeneous deformation resulting in barreling of the compressed micropillars. No clear differences in the outer shape of micropillars could be identified as a function of strain rate or temperature. TKD analysis (Figs. 7a and 8a) was performed on the FIB lift-out lamellae of undeformed as well as deformed micropillars. For each lamella, between 358 and 809 individual grains were identified in the TKD maps far exceeding the recommended minimum number for EBSD-based grain size measurement according to ASTM E2627 [52]. This analysis revealed that although the average grain area did not change between undeformed and deformed pillars (Fig. 7d for cumulative grain size distribution), the grain ellipticity changed from 0.865 ± 0.023 in undeformed to 0.838 ± 0.003 in deformed micropillars (average grain aspect ratios 1.99:1 and 1.83:1, respectively). This means that the deformed micropillars featured less elongated grains com-

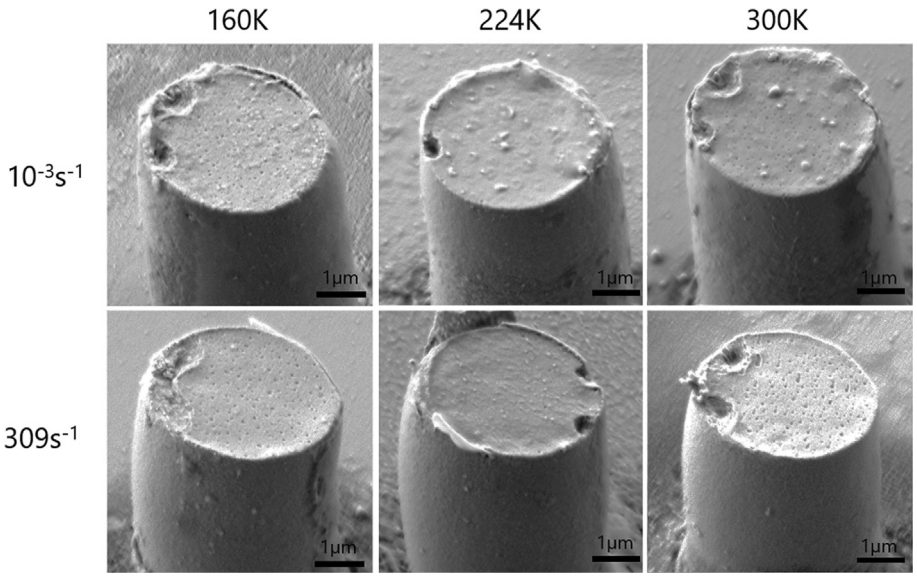

Fig. 6. HRSEM images of deformed micropillars following experiments at 160 K (left), 224 K (middle), and 300 K (right) at quasistatic (top) and high strain rates (bottom). Please note that the origin of impressions at the specimen top is attributed to defects stemming from the manufacturing process, as shown in the undeformed case (Supplementary Fig. 2). Also, the outer rim sticking out from the micropillars is due to the breaking of the gold thin film (10 nm thick) coated on the nickel micropillars. Such a coating was required to avoid charging of the samples from the electron beam during mechanical testing, as the electrodeposited micropillars were glued onto the aluminum SEM stub using electrically non-conductive glue.

pared to the undeformed microstructure, which is in line with a qualitative assessment of IPF colour maps (Fig. 7a). No significant variation in grain ellipticity was found as a function of testing conditions.

Grain orientation analysis (Fig. 7c) showed a change in misorientation distribution from the as deposited to the deformed micropillars. In the undeformed material, grains were preferentially elongated parallel to the pillar axis. The deformed micropillars featured a more homogeneous alignment distribution close to the theoretical random distribution featuring three weak peaks at 15°, 45°, and 75° (Fig. 7c). This is a significant change from the as deposited state and agrees with our subjective interpretation of IPF colour maps (Fig. 7a) that the grains in the deformed micropillars were less aligned with, or less elongated in, the growth direction.

Texture analysis from TKD data relative to the vertical, loading direction of the pillars (Fig. 7b) showed that the dominant texture parallel to the loading direction changed from approximately {1 1 3} in the undeformed material to {1 1 0} in the deformed micropillars. This change in texture occurred irrespective of the temperature or strain rate at which the experiments were performed. However, it was found that a trace of the original texture remained also in the deformed micropillars. This remaining trace was more strongly visible for micropillars deformed at lower temperatures and higher strain rates.

Grain and twin boundaries were further quantified based on TKD data (Fig. 8). It was found that for the undeformed material, 29 ± 1.2% (by length) of all boundaries were Σ3 twin boundaries (TB), whilst 68 ± 1.5% were non-twin high angle grain boundaries (HAGB, >15° misorientation) and 3 ± 0.4% were low angle grain boundaries (LAGB, misorientation between 5° and 15°). No other coincident site lattice boundaries (from Σ3 to Σ29) were measured to substantially exceed the expected distribution for a random texture. In deformed micropillars, the relative proportion of TB decreased to 21 ± 2.9% for room temperature and 14 ± 2.7% for cryogenic temperatures, whilst LAGB increased to approximately 4.7 ± 1.2% for room temperature and 6 ± 1.2% for cryogenic temperature; hence, HAGB also increased to 74 ± 2.6% for room temperature and 80 ± 2.8% for cryogenic temperature (Fig. 8b). It was furthermore found that the area fraction of grains containing twin boundaries decreases from 57 ± 10% in the as deposited micropillars to 22–41% (Fig. 8c) in the deformed ones depending on the applied temperature and strain rate. Due to the scatter in the data, no clear trend could be identified for the fraction of twinned grains as a function of temperature or strain rate.

Five ncNi microlattices (Fig. 9a) were compressed at different strain rates from 0.0006/s to 0.06/s inside an SEM, (Fig. 9b, supplementary video V1). Only small strain rate sensitivity was found with the microlattice effective yield stress varying between 410 MPa and 420 MPa for the strain rate range 0.0006/s to 0.06/s. Finite element simulations predict a yield stress of approximately 310 to 490 MPa depending on the strut width of the simulated unit cell for a strain rate of 0.06/s and localization of plastic deformation in the struts near the junctions (Fig. 9d and 8e) in agreement with the experimentally observed failure locations.

4. Discussion:

The TAE process used in this study resulted in a highly reproducible, taper-free micropillar shape (Fig. 3a). The structures are free of artifacts induced by FIB milling, which can result in grain growth, amorphization, and ion implantation near the surface. Furthermore, APT revealed a high purity of the deposits of 99.68% nickel and impurities, mainly oxygen/sulfur, segregating at grain boundaries. These elements are known to have an embrittling effect on the mechanical performance of ncNi and are often found in deposits from sulfamate baths.

XRD analysis showed no clear texture and average grain size of ~ 30 nm; TEM and TKD analysis of FIB lift-out lamellae from undeformed micropillars revealed a columnar grain structure with an aspect ratio of 2:1 and a minimum grain dimension of ~ 30 nm. The discrepancies arise due to the difference in the probed volumes of the three methods (bulk for XRD vs. local pillar for TKD/TEM) and the direction of analysis (in-plane for XRD vs transverse for TKD/TEM). As shown by numerical simulations of the electrodeposition process (Fig. 3d), the main growth direction of the deposition process changes significantly between the confined micropillar and the free growth of the bulk substrate. Grains are expected to be

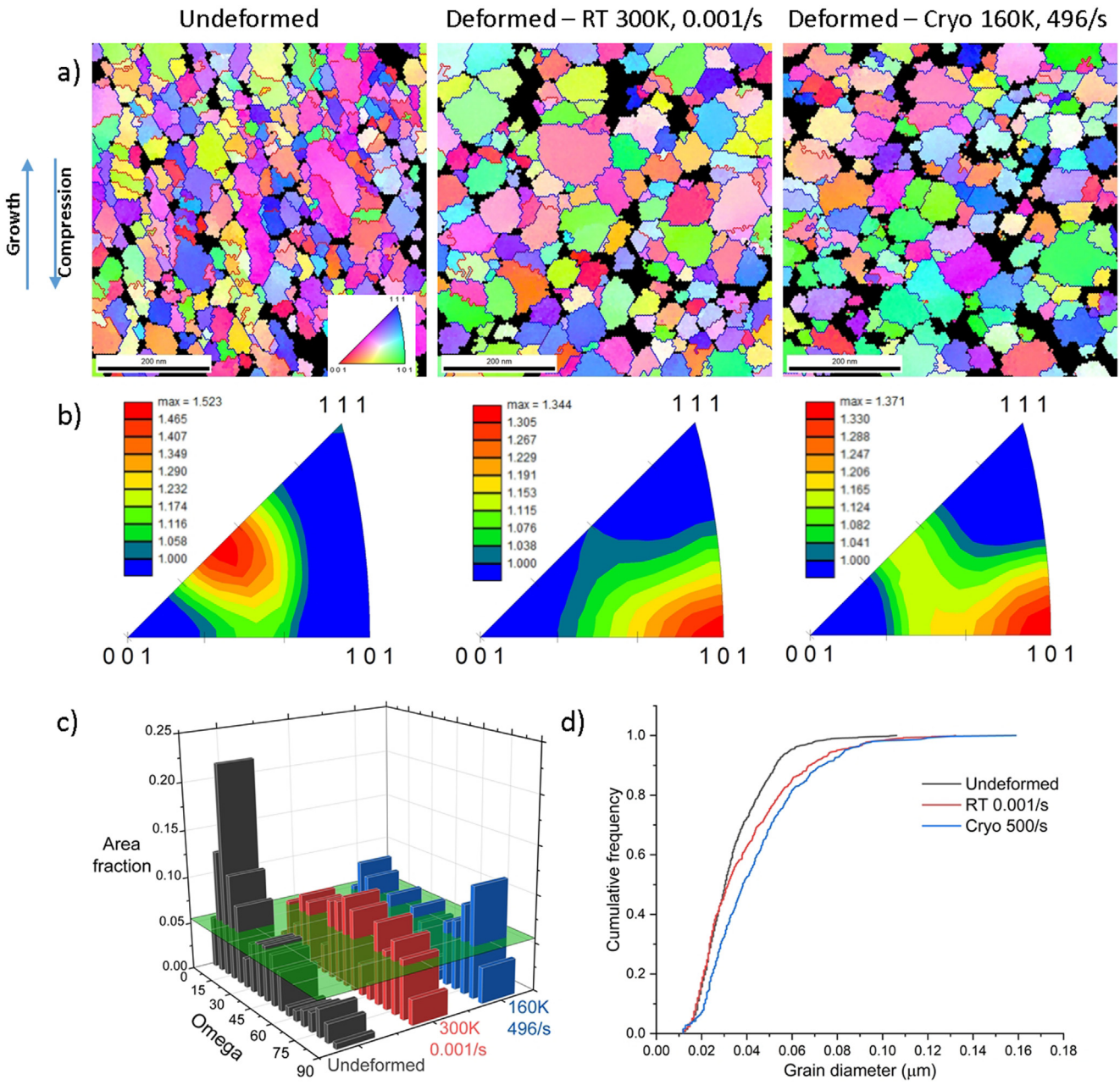

Fig. 7. a) TKD inverse pole figure colour maps (the IPF colour scale is shown at the bottom of the left figure. Blue lines signify high angle grain boundaries, purple lines low angle boundaries and red lines Σ3 twin boundaries; black points are unindexed. b) TKD texture analysis in the vertical direction of FIB lift-out lamellae from an undeformed micropillar (left), a micropillar loaded at 300 K at quasistatic strain rate (middle), and a micropillar deformed at 160 K and high strain rate (right). c) Orientation distribution of the major axes of the grains determined by TKD for undeformed and deformed micropillars as a function of temperature and strain rate. The vertical axis shows the respective area-weighted fraction as a function of the angle of the major axis of the grain with respect to the horizontal direction (0° corresponds to an alignment of the grain long axis with the loading direction). The green plane represents the expected orientation distribution for random grain orientation. d) Cumulative grain size distribution in the undeformed and deformed samples under different loading conditions.

elongated in the growth direction, aligned, and feature a texture within the micropillar, as the growth front is planar. Once the micropillar mold is filled, the growth front becomes approximately a half-sphere. Therefore, texture and grain alignment cannot be measured by XRD, which samples over a large volume of interest and therefore averages out local texture variations in the bulk. Furthermore, the predicted increase in current density by ~ 1% (<1 mA/cm^2) when comparing growth inside a mold with free growth of the bulk substrate is not large enough to effect drastic changes in deposit microstructure that typically require changes in current density by at least 10 mA/cm^2 [53]. The overall high current density is an indication of columnar growth, which is in line with the TKD data. For this reason, we stipulate that in this case TKD and TEM are more suitable techniques for studying the microstructure of templated micropillars than XRD due to the possibility to perform local measurements.

Here, a new *in situ* nanoindenter was developed and utilized that allows performing micromechanical experiments at subambient temperatures and in a wide range of strain rates inside an SEM. It should be emphasized that this is the first time that the mechanical properties of ncNi could be ascertained in this range of temperatures and strain rates at the microscale. Despite the

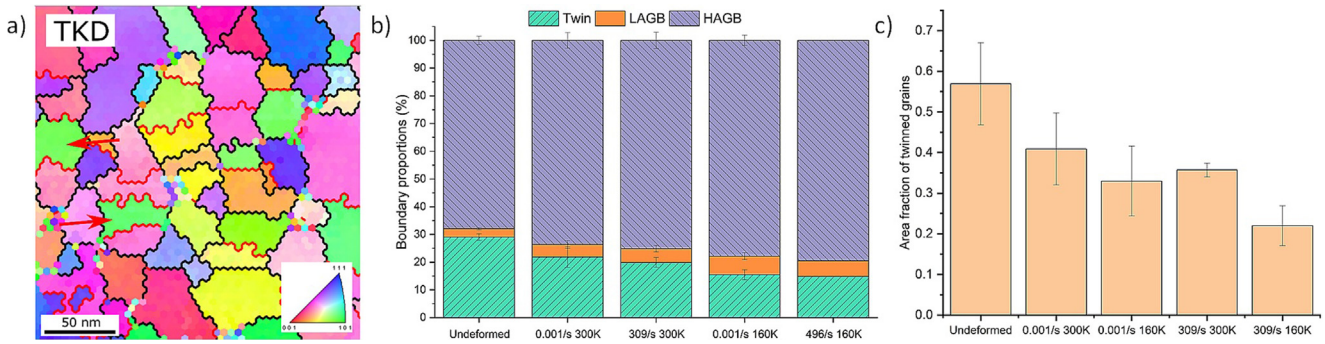

Fig. 8. TKD map (coloring relative to loading axis) of coarse growth twins with twin boundaries highlighted in red, other grain boundaries in black. b) Proportion (in length) of TB, HAGB, and LAGB of all boundaries for undeformed and deformed micropillars as a function of temperature and strain rate. c) Area fraction of twinned grains compared between undeformed and deformed samples tested under a variety of temperatures and strain rates.

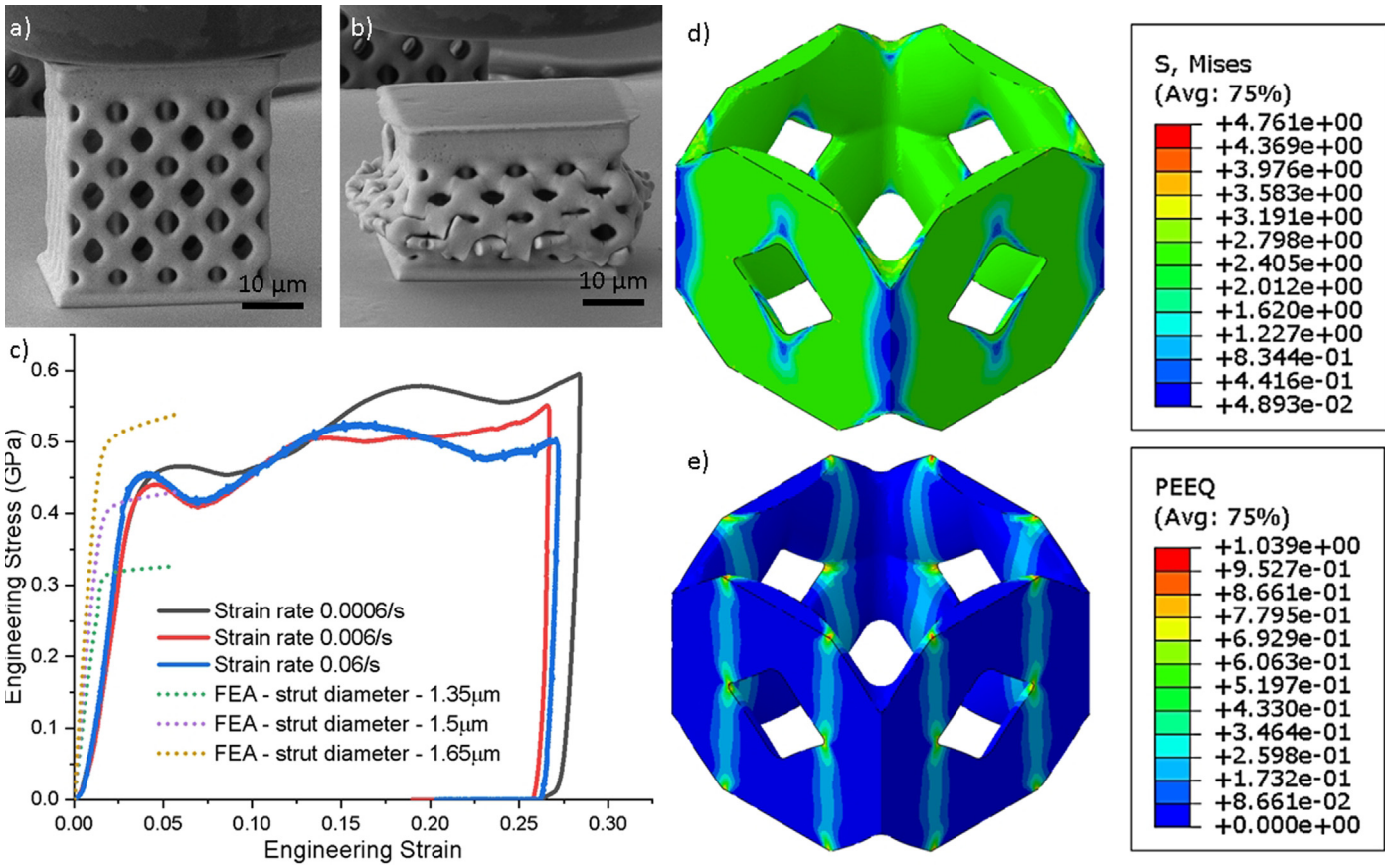

Fig. 9. ncNi microlattices a) before and b) after compression at a strain rate of 0.0006/s. Representative stress–strain signatures of the ncNi microlattice compressions at different strain rates and FEM simulations are shown in c). FEM simulations conducted on the microlattice unit cells show the distribution of d) von Mises stress levels and e) equivalent plastic strain. Stresses are reported in GPa.

overall low strain rate sensitivity of the tested material, m could be reliably extracted due to the large number of experiments and wide range of strain rates that can be probed using the novel setup.

Previous studies conducted on ncNi with a similar crystallite size of $\sim$ 30 nm have identified a slightly higher strain rate sensitivity m of $\sim$ 0.01 [21,32,33,37,54] compared to what was found here. However, it should be noted that the m values reported in these studies were either determined at a narrower strain rate range between 10^{-5} and 0.01/s. In contrast, the strain rate sensitivity in this study has been calculated from yield stress values measured in monotonic experiments conducted over a wide range of strain rates (0.001 to 500/s). Rajaraman et al. [32], who performed rate dependent macroscale tests on ncNi, report a strain rate sensitivity coefficient m of 0.007 between 0.004 and 3093/s, well in line with what has been reported here. In this study and a few others [32,33], dynamic recrystallization was hypothesized to occur at strain rates above $\sim$ 1000/s, increasing the strain rate sensitivities significantly, but such ultra high strain rates are beyond the scope of this current study.

It should be noted that Lohmiller et al, have previously conducted macroscale room temperature quasi-static compression on ncNi with 30 nm grain size and obtained a strength level of $\sim$ 1.6GPa, which suggests the presence of tension/compression

strength asymmetry in ncNi when compared to the study by Wang et al. [37,55]. In terms of deformation mechanism, Lohmiller et al identified a three-stage process for quasi-static testing, where the system evolves sequentially from elastic to dislocation plasticity to stress-driven grain growth at large strains (~20%). In the current study though, at similar strain levels, regardless of the speed (or strain rate) and the temperature of testing, we did not observe stress-driven grain growth even at large strains. At this point, the reason for this difference in deformation mechanisms is not clear, but it could potentially stem from differences in electrodeposition conditions (pulsed vs. direct current) and electrolyte composition. Regardless, the increase in yield stress with decreasing temperature points towards a thermally activated deformation process during the compression of ncNi micropillars.

To shed light on the rate limiting mechanism, we calculated the apparent activation volume, which was found to decrease from approximately $122b^3$ at 300 K (similar to previous room temperature studies [21,37]) to $59b^3$ at 240 K and $45b^3$ at 160 K (Fig. 5d). In the activation volume range of 10-100b^3 several plausible deformation mechanisms can operate in parallel, including dislocation-grain boundary interactions and grain boundary diffusion. Previous *in situ* mechanical testing inside the TEM studies of ncNi with a grain size of $\sim$ 30 nm has determined dislocation nucleation from grain boundaries and triple junctions as the dominant mechanism behind deformation at quasi-static strain rates [56]. In addition, as the temperature is lowered to cryogenic levels and experimental time-scales are lowered to hundreds of microseconds (at $\sim$ 500/s strain rate), it is conceivable that the contribution of diffusion (given a typical grain boundary diffusion strain rate of $\sim 10^{-8}$/s in ncNi with 20 nm grains at room temperature [57]), if any, is diminished even further. Therefore, we hypothesize that especially at subambient temperatures, the plasticity of ncNi is predominantly controlled by the collective dislocation nucleation/propagation-based dislocation-grain boundary interactions. Asaro et al [48], using mechanistic models, determined that in ncNi with grain size >15 nm, the deformation process more likely involves the emission of partial dislocations from the grain boundaries or triple points [48]. Using their models (equations 5 and 19 of [48]), for a grain size of 30 nm (corresponding to the smallest dimension of the elongated grains in this work), a flow stress value between $\sim$ 2.1 GPa to 3.1 GPa can be estimated for a thermally activated partial dislocation based deformation mechanism. The yield stress measured in our current study on ncNi with a minimum grain thickness of 30 nm (2.75 GPa and 2.5 GPa at cryo and room temperatures, respectively) falls within the predicted range of flow stresses, further supporting the hypothesis of dislocation emission from grain boundary or triple point as the dominant rate-controlling mechanism.

Grain boundary mediated dislocation emission is indeed a thermally activated process that becomes increasingly difficult as the temperature is lowered to cryogenic levels [58]. This would explain the increase in the compressive yield strength for ncNi at 160 K and 240 K compared to room temperature, across all the strain rates, as seen in Fig. 5c). Another interesting characteristic of the stress–strain curves reported in Fig. 5a) and b), is the lack of strain hardening in the plastic regime under all conditions of strain rate and temperature. This can be explained by the small grain size of $\sim$ 30 nm. The grains are in this case too small for dislocation pile-up or other dislocation reactions to occur even at high strain rates, which is susceptible to higher dislocation density as mentioned above. Using Orowan's relation for expansion of dislocation loops it has been previously calculated that the grain size for nickel needs to be above 38 nm for the occurrence of dislocation multiplication [59], which is in line with our experimental findings.

Furthermore, apparent activation energy was calculated and found to be 57 kJ/mol or 0.59 eV. This is far lower than the grain boundary and lattice diffusion in nickel, which are on the order of $\sim$ 1.19 eV and $\sim$ 2.94 eV, respectively [21]. Peng et al [60] have previously conducted nudged elastic band simulations to identify the activation energy required for partial dislocation nucleation from the surface in nickel as $\sim$ 0.7 eV, which was experimentally confirmed by Wang et al. using tensile experiments at cryogenic temperatures on ncNi with 30 nm grain size [61] and is close to the activation energy of 0.59 eV identified in this study.

Texture analysis from TKD data (Fig. 7b) showed that the dominant texture in the loading direction changed during deformation irrespective of the testing temperature and strain rate. However, a trace of the original texture remained also in the deformed micropillars, with a trend that the trace was more strongly visible for micropillars deformed at lower temperatures and higher strain rates. This is in principle an expected outcome, as (1 1 0) is the deformation texture resulting from large compressive deformation in fcc metals [62]. The fact that the deformation texture was less dominant for higher strain rates and lower temperatures is in line with the activation of glide systems with a lower Schmid factor at high strain rates, as a higher number of dislocation sources is required to accommodate the fast plastic deformation. These non-Schmid glide planes hence prevent a classical texture formation under high strain rate loading.

Different deformation mechanisms have been suggested for nanocrystalline metals in the past including partial dislocation mediated processes (PDMP) like deformation twinning, formation of extended and full dislocations from grain boundaries, grain boundary sliding, or grain rotation [63]. Dislocation activity was observed in *in situ* TEM studies [64], but not in post-mortem TEM studies of tensile ncNi samples deformed at room temperature. This may be explained by the annihilation of dislocations at the grain boundaries. However, post-mortem observation of nanotwins and dislocations is possible on ncNi specimens deformed at liquid nitrogen temperatures, where a high density of mechanical twins and stacking faults have been observed in previous studies [65]. The presence of Shockley partial dislocations at the front of the stacking faults stopping in the grain interior shown in previous work suggests that the twins nucleate heterogeneously at the grain boundaries and grow into the grain interior by emission of partial dislocations. In nickel grains with a diameter > 27 nm, dissociated full dislocations nucleate at a lower stress than partial dislocations at room temperature. Once nucleated, the extended dislocation has short splitting distances between the two Shockley partials and behaves like a perfect dislocation [49].

The fact that we do not see deformation twins may be explained by the small grain size in combination with the temperature at which the experiments were performed. Nanotwins and dislocations have only been observed in ncNi after experiments at liquid nitrogen temperature. While we performed experiments at subambient temperatures and high strain rates, it is possible that the conditions were not optimal to trap dislocations in the grains as was shown for liquid nitrogen temperature. On the other hand, it is also possible that eventual mechanical nanotwins that develop in nanocrystalline materials at low temperatures and high strain rates, in addition to the growth twins, could not be observed using the methods employed in this study due to their limited spatial resolution, e.g. the 5 nm step size for TKD, as seen in Fig. 7. However, HR-TEM analysis (Fig. 10a) also did not show clear evidence of deformation twinning in the compressed micropillars, representatively shown in Fig. 10b to 10d; any lath features further refined than the growth twins were found to be associated with Moiré fringes arising from grain overlap. Recently, a study identified that in single crystalline copper and copper alloys, twinning is favored at low stacking fault energy (SFE) materials. In the current study, given nickel has a higher SFE compared to other FCC metals such as copper, deformation twinning is not expected. As confirmation,

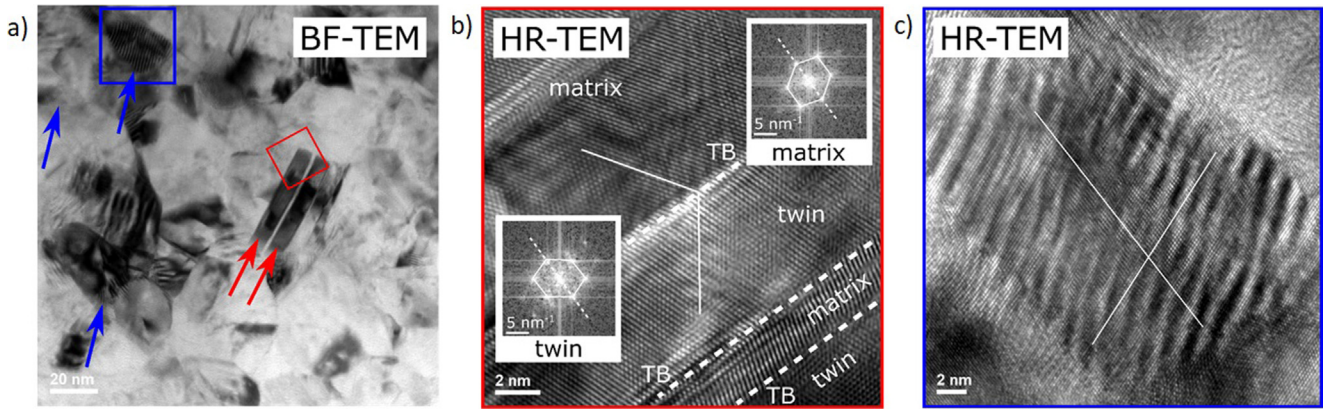

Fig. 10. a) Bright field TEM images of undeformed and deformed samples tested at different loading conditions. High resolution imaging of twin and resembling features in a quasi-statically tested sample under room temperature conditions: b) bright field TEM image of coarse twins (red arrow), and other more refined lath features (blue arrows), c) coarse twins and d) Moiré fringes identified as the lath features using HR-TEM, that are associated with grain overlap (no twin-type mirroring of atomic lattice across grain – white lines are a guide to the eye), rather than being a deformation twin.

TKD and TEM inspections on samples tested at high strain rate and cryogenic temperature combinations revealed a lack of deformation twins [66].

The electrodeposited ncNi used in this study features initially a combination of LAGBs, HAGBs and coherent twin boundaries (CTBs), as seen from the TKD analysis of the undeformed sample shown in Fig. 8b). It is also clear that the majority of the boundaries are either HAGBs or CTBs. After deformation, regardless of the temperature and strain rate, there is a decrease in CTB percentage and an increase in the HAGB percentage (Fig. 8b), but no apparent grain size change was observed (Fig. 7d). In general, in nanocrystalline fcc metals, there is a competition between twinning and detwinning during mechanical loading. It has been determined in previous studies that if the grain size is between 45 and 100 nm twinning is preferred, while for grain sizes outside this range detwinning dominates [67]. It should be noted that this specific study from the literature was conducted on a Ni-Fe alloy system. Therefore, in the current study with 30 nm nickel grains (smallest dimension of the elongated grains), while detwinning of CTB is likely to occur under compression, the exact cutoff of grain size required for twinning and detwinning still needs to be determined. Detwinning is a twin boundary migration process, by Shockley partial dislocations traveling across the grain, while twinning happens when a nucleus initiates at a grain boundary and propagates across the grain. Thus, during deformation, we hypothesize that as the first step, partial dislocations emit from HAGB ledges. This is because it is easier for HAGBs to emit dislocations from the GB ledges than LAGBs [68], and at yield, the initial dislocation density can even be solely attributed to the dislocations sourced from the GB ledges. In the second step, the nucleated partials react with the existing CTBs and the HAGBs on the opposite end of the grain. It has been shown previously that the accumulation of dislocations can transform an existing CTB into a curved incoherent HAGB [69]. Theoretical estimation of dislocation nucleation rate based on equations (2) and (3) [70,71] was also carried out using the estimated activation volume V_{app} determined at different temperatures and a Young's modulus E of approximately 180GPa.

$$v = Nv_0 \exp\left(-\frac{Q(\sigma_y,T)}{k_B T}\right) \tag{2}$$

$$\frac{Q(\sigma_y,T)}{k_B T} = \ln\frac{k_B T N v_0}{E\dot{\varepsilon}V_{app}(\sigma_y,T)} \tag{3}$$

where N is the number of dislocation nucleation sites (which remains constant across samples), v_0 is the attempt frequency (~Debye frequency of 10^{12}/s [72]), Q is the activation free energy, σ_y is the yield stress, and $\dot{\varepsilon}$ is the strain rate. At room temperature, we found the dislocation nucleation rate to vary from 15.7/s to 7.80×10^6/s depending on the strain rate in the range from 0.001 to 500/s. Similarly, at a low temperature of 160 K the dislocation nucleation rate predicted varies between 10.9/s and 5.39×10^6/s in the same range of strain rates. Based on this, we estimate a ratio of 1.45 in the dislocation nucleation rate of ncNi micropillars between room temperature and cryogenic temperatures. As such, at higher strain rates a significant increase in dislocation nucleations could be expected at all temperatures. From Fig. 8b) it can be seen that at high strain rates, the CTB percentages decline and HAGB percentages increase more compared to quasi-static tests, both at room and cryogenic temperatures. This can be attributed to the significant increase in dislocation nucleation rates and in turn the larger number of dislocations at higher strain rates. Thus, during high strain rate experiments with enhanced dislocation nucleations, more reactions of partials with CTBs and their transformation to HAGBs can be expected [73]. Though it should be noted that even at higher strain rates with the significantly higher dislocation nucleations expected, there is a lack of change in apparent hardening compared to tests conducted at lower strain rates, as evident from the stress–strain signatures (see Fig. 5a) and b)). This shows that the dislocations are unable to interact with each other owing to the nanocrystalline grain size of ~ 30 nm [74], regardless of the testing conditions.

Given that the thermally activated deformation processes are significantly affected by a complex interplay of strain rate and temperature, the Zener-Hollomon parameter 'Z' is typically used in such to capture their combined effect. The 'Z' parameter is obtained using the following equation:

$$Z = \dot{\varepsilon}\exp(Q/RT)$$

where $\dot{\varepsilon}$ is the strain rate, Q is the activation energy, R is the gas constant and T is the temperature. Using the activation energy extracted from the thermal activation analysis based on the stress–strain curves, the 'ln Z' parameter was calculated to vary from 16 to 49, as the strain rate and temperature are varied from 0.001/s to 496/s and 300 K to 160 K, respectively. Previous studies on microcrystalline nickel showed that at low strains, when the ln Z parameter varies from 20 to 60, dynamic recrystallization occurs resulting in grain growth or nucleation [75]. A recent study on microcrystalline copper showed that when the ln Z parameter is between 36 and 48 twinning or nanotwin-assisted dynamic recrystallization occurs [76]. Interestingly, from the current study, we did not observe any deformation mechanism change including twin-

ning or nanotwin formation or recrystallization as the lnZ parameter was varied between 16 and 49. This could be attributed to the nanocrystalline grain size of our nickel deposits. The only quantifiable microstructural change observed was at the combination of high strain rate (496/s) and cryogenic temperature (160 K) with a lnZ of 49, where it was found that the deformed micropillar had retained a trace of the original texture, while in all the other cases a change of texture from {1 1 3} to {1 1 0} occurred.

With regards to 3D microlattices, as seen in Fig. 9a), near-ideal connectivity was achieved at the nodes, a prerequisite for achieving good mechanical properties. However, it should also be noted that the exact geometry of the fabricated lattices differs from the intended design, especially at the nodes, where a larger than expected thickness was achieved due to inaccuracies in the multi-step synthesis process. This is likely caused by the laser parameters used for obtaining the templating molds. Therefore, further optimization of the TAE technique using different laser powers for struts and nodes is required to exactly replicate the designs in the future. Concerning their mechanical properties (see Fig. 9c), ncNi microlattices show a high yield strength $\sim$ 410–420 MPa at all strain rates, followed by oscillations in apparent flow stress, indicative of layer-by-layer collapse (see Fig. 9b) and supplementary video V1). Also, from the supplementary video V1, it can be seen that the plastic deformation in the lattices localizes in the struts near the junctions where the bending load is the highest.

Using a range of strut dimensions (elliptical shape – 1.35 μm to 1.65 μm minor axis and 2.7 μm to 3.3 μm major axis) of the printed ncNi microlattices identified via SEM imaging, 3D models of the unit cell of the microlattice were constructed with different strut dimensions. Uniaxial compression experiments were simulated using FEM by applying kinematic uniform boundary conditions (KUBC) to mimic the effect of the surrounding periodic structure [77]. The yield stress range obtained using FEM simulations lies between 310 and 490 MPa depending on the considered strut dimensions, which is in line with the experimental yield stress of approximately 410 MPa. This shows that within the significant uncertainty of the exact geometry of the printed structures, FEM simulations can predict a range of apparent properties consistent with experiments. Furthermore, in line with the failure locations identified in the experiment, it was found that plastic deformation localized vertically in the struts near the junctions (Fig. 9d and 9e). The fact that the deformation and failure mechanisms are captured by the finite element model of the microlattice unit cell is promising and shows the potential of this approach for the knowledge-based design of complex structures. By realizing a tighter control of the final geometry through optimization of process parameters during the multistep synthesis process as well as an accurate estimation of the exact geometry, flaws, and structural defects via high resolution imaging techniques such as synchrotron based computed nanotomography [78], the quantitative correlation of mechanical properties can be improved further in future studies.

5. Conclusion:

In this study, two-photon lithography was combined with template assisted electrodeposition to produce a ncNi sample array consisting of thousands of micropillars enabling high throughput analysis. A novel *in situ* nanoindenter setup was developed, allowing for the first time, to perform compression experiments at sub-ambient temperatures (160 K to 300 K) and in a large range of strain rates (0.001 to 500/s) inside an SEM. Consistently high yield stresses were measured ranging between 2.4 GPa and 3.2 GPa and the highest yield stresses were found for the samples tested at a strain rate of $\sim$ 500/s at 160 K. The strain rate sensitivity and thermal activation analysis resulted in the hypothesis of collective nucleation of dislocations at grain boundaries being the dominant rate limiting deformation mechanism, gaining in relative importance compared to grain boundary diffusion at lower temperatures. Further analysis using TEM and TKD of compressed and pristine micropillars highlighted the microstructural changes due to compressive deformation of the ncNi. Significant reduction in grain elongation and a relative increase in the proportion of high angle grain boundaries vs. Σ3 twin boundaries were observed. Furthermore, a clear change in texture was found in most of the deformed samples, where it was less pronounced on specimens deformed at lower temperatures and higher strain rates. This study thus investigated the deformation mechanisms and texture evolution during compressive deformation of ncNi. Furthermore, we determined the baseline rate- and temperature-dependent constitutive properties of template-assisted electrodeposited ncNi microscale structures, which is an attractive technique due to its high precision, purity, and potential scalability. Finally, the rate-dependent compression properties of complex ncNi microlattices were ascertained experimentally at intermediate strain rates upto 0.06/s, along with FEM simulations of the microlattice unit cell based on the constitutive model extracted from the micropillar compressions, which was able to reproduce the observed yield stress range and failure mode. This study is thus intended as a baseline for future efficient design of metallic metamaterials highly relevant for applications such as lightweight design for space flight and aviation based on the combination of experimental and computational approaches.

Declaration of Competing Interest

The authors declare that they have no known competing financial interests or personal relationships that could have appeared to influence the work reported in this paper.

Acknowledgements

JS and RR would like to thank Damian Frey (Alemnis AG) for his valuable support during setup development. JS acknowledges funding through Swiss National Science Foundation Ambizione grant no. 174192. RR acknowledges funding from the EMPAPOSTDOCS-II program funded by the European Union's Horizon 2020 research and innovation program under the Marie Skłodowska-Curie grant agreement number 754364.

Data availability

Data will be made available upon reasonable request.

Appendix A. Supplementary material

Supplementary data to this article can be found online at https://doi.org/10.1016/j.matdes.2022.110836.

References

[1] F. Ebrahimi, G.R. Bourne, M.S. Kelly, T.E. Matthews, Mechanical properties of nanocrystalline nickel produced by electrodeposition, Nanostruct. Mater. 11 (1999) 343–350, https://doi.org/10.1016/s0965-9773(99)00050-1.
[2] E.W. Backer, W. Ehrfeld, D. Münchmeyer, H. Betz, A. Heuberger, S. Pongratz, W. Glashauser, H.J. Michel, R. v. Siemens, Production of separation-nozzle systems for uranium enrichment by a combination of x-ray-lithography and galvanoplastics, Naturwissenschaften 69 (11) (1982) 520–523.
[3] T.A. Schaedler, A.J. Jacobsen, A. Torrents, A.E. Sorensen, J. Lian, J.R. Greer, L. Valdevit, W.B. Carter, Ultralight metallic microlattices, Science 334 (2011) 962–965, https://doi.org/10.1126/science.1211649.

[4] M.Q. Wang, X.G. Wang, Electrodeposition zinc-oxide inverse opal and its application in hybrid photovoltaics, Sol. Energy Mater. Sol. Cells 92 (2008) 357–362, https://doi.org/10.1016/j.solmat.2007.10.001.

[5] J. Fischer, M. Wegener, Three-dimensional optical laser lithography beyond the diffraction limit, Laser Photonics Rev. 7 (2013) 22–44, https://doi.org/10.1002/lpor.201100046.

[6] J.K. Gansel, M. Thiel, M.S. Rill, M. Decker, K. Bade, V. Saile, G. von Freymann, S. Linden, M. Wegener, Gold helix photonic metamaterial as broadband circular polarizer, Science 325 (2009) 1513–1515, https://doi.org/10.1126/science.1177031.

[7] X.W. Gu, J.R. Greer, Ultra-strong architected Cu meso-lattices, Extreme Mech. Lett. 2 (2015) 7–14, https://doi.org/10.1016/j.eml.2015.01.006.

[8] P. Schuerch, L. Petho, J. Schwiedrzik, J. Michler, L. Philippe, Additive manufacturing through galvanoforming of 3D nickel microarchitectures: Simulation-assisted synthesis, Advanced Materials Technologies. 3 (2018) 8, https://doi.org/10.1002/admt.201800274.

[9] P. Schuerch, R. Ramachandramoorthy, L. Petho, J. Michler, L. Philippe, Additive manufacturing by template-assisted 3D electrodeposition: Nanocrystalline nickel microsprings and microspring arrays, Applied, Mater. Today (2019), https://doi.org/10.1016/j.apmt.2019.100472 100472.

[10] C.V. Manzano, P. Schurch, L. Petho, G. Burki, J. Michler, L. Philippe, High aspect-ratio nanocrystalline CuNi T-structures and micro-gears: Synthesis, numerical modeling and characterization, J. Electrochem. Soc. 166 (2019) E310–E316, https://doi.org/10.1149/2.0961910jes.

[11] D. Jia, K.T. Ramesh, E. Ma, L. Lu, K. Lu, Compressive behavior of an electrodeposited nanostructured copper at quasistatic and high strain rates, Scr. Mater. 45 (2001) 613–620, https://doi.org/10.1016/S1359-6462(01)01071-5.

[12] J.D. Giallonardo, U. Erb, K.T. Aust, G. Palumbo, The influence of grain size and texture on the Young's modulus of nanocrystalline nickel and nickel–iron alloys, Phil. Mag. 91 (2011) 4594–4605, https://doi.org/10.1080/14786435.2011.615350.

[13] M.D. Uchic, D.M. Dimiduk, A methodology to investigate size scale effects in crystalline plasticity using uniaxial compression testing, Mater. Sci. Eng.: A 400 (2005) 268–278.

[14] X. Maeder, W.M. Mook, C. Niederberger, J. Michler, Quantitative stress/strain mapping during micropillar compression, Phil. Mag. 91 (7-9) (2011) 1097–1107.

[15] S. Korte, W.J. Clegg, Micropillar compression of ceramics at elevated temperatures, Scr. Mater. 60 (9) (2009) 807–810.

[16] D. Kiener, P.J. Guruprasad, S.M. Keralavarma, G. Dehm, A.A. Benzerga, Work hardening in micropillar compression: In situ experiments and modeling, Acta Mater. 59 (10) (2011) 3825–3840.

[17] L. Han, L. Wang, J. Song, M.C. Boyce, C. Ortiz, Direct quantification of the mechanical anisotropy and fracture of an individual exoskeleton layer via uniaxial compression of micropillars, Nano Lett. 11 (9) (2011) 3868–3874.

[18] R. Schwaiger, M. Weber, B. Moser, P. Gumbsch, O. Kraft, Mechanical assessment of ultrafine-grained nickel by microcompression experiment and finite element simulation, J. Mater. Res. 27 (1) (2012) 266–277.

[19] J. Schwiedrzik, R. Raghavan, A. Bürki, V. LeNader, U. Wolfram, J. Michler, P. Zysset, In situ micropillar compression reveals superior strength and ductility but an absence of damage in lamellar bone, Nat. Mater. 13 (2014) 740–747.

[20] G. Mohanty, J. Wehrs, B.L. Boyce, A. Taylor, M. Hasegawa, L. Philippe, J. Michler, Room temperature stress relaxation in nanocrystalline Ni measured by micropillar compression and miniature tension, J. Mater. Res. 31 (2016) 1085–1095, https://doi.org/10.1557/jmr.2016.101.

[21] G. Mohanty, J.M. Wheeler, R. Raghavan, J. Wehrs, M. Hasegawa, S. Mischler, L. Philippe, J. Michler, Elevated temperature, strain rate jump microcompression of nanocrystalline nickel, Phil. Mag. 95 (16-18) (2015) 1878–1895.

[22] C.L. Wang, Y.H. Lai, J.C. Huang, T.G. Nieh, Creep of nanocrystalline nickel: A direct comparison between uniaxial and nanoindentation creep, Scr. Mater. 62 (2010) 175–178, https://doi.org/10.1016/j.scriptamat.2009.10.021.

[23] D. Kiener, C. Motz, M. Rester, M. Jenko, G. Dehm, FIB damage of Cu and possible consequences for miniaturized mechanical tests, Mater. Sci. Eng.: A 459 (2007) 262–272, https://doi.org/10.1016/j.msea.2007.01.046.

[24] G. Schoeck, The activation energy of dislocation movement, Physica Status Solidi (b). 8 (2) (1965) 499–507.

[25] R.E. Robertson, Theory for the plasticity of glassy polymers, J. Chem. Phys. 44 (10) (1966) 3950–3956.

[26] C.A. Schuh, J.K. Mason, A.C. Lund, Quantitative insight into dislocation nucleation from high-temperature nanoindentation experiments, Nat. Mater. 4 (8) (2005) 617–621.

[27] J. Wheeler, C. Niederberger, C. Tessarek, S. Christiansen, J. Michler, Extraction of plasticity parameters of GaN with high temperature, *in situ* micro-compression, Int. J. Plast. 40 (2013) 140–151.

[28] J. Wehrs, M.J. Deckarm, J.M. Wheeler, X. Maeder, R. Birringer, S. Mischler, J. Michler, Elevated temperature, micro-compression transient plasticity tests on nanocrystalline Palladium-Gold: Probing activation parameters at the lower limit of crystallinity, Acta Mater. 129 (2017) 124–137, https://doi.org/10.1016/j.actamat.2017.02.045.

[29] H. Li, T. Chen, W. Li, H. Zhang, S. Han, C. Zhou, Z. Chen, E.A. Flores-Johnson, L. Shen, J. Lian, I.J. Beyerlein, X. Liao, Grain size dependent microstructure and texture evolution during dynamic deformation of nanocrystalline face-centered cubic materials, Acta Mater. 216 (2021), https://doi.org/10.1016/j.actamat.2021.117088 117088.

[30] R.T. Zhu, X.X. Zhang, Y.F. Li, J.Q. Zhou, Impact behavior and constitutive model of nanocrystalline Ni under high strain rate loading, Mater. Des. 49 (2013) 426–432, https://doi.org/10.1016/j.matdes.2013.01.060.

[31] X.L. Wu, Y.T. Zhu, Inverse Grain-Size Effect on Twinning in Nanocrystalline Ni, Phys. Rev. Lett. 101 (2008), https://doi.org/10.1103/PhysRevLett.101.025503 025503.

[32] S. Rajaraman, K.N. Jonnalagadda, P. Ghosh, in: V. Chalivendra, B. Song, D. Casem (Eds.), Dynamic Behavior of Materials, 1, Springer, New York, New York, NY, 2013, pp. 157–163, https://doi.org/10.1007/978-1-4614-4238-7_20.

[33] F. Dalla Torre, H. Van Swygenhoven, M. Victoria, Nanocrystalline electrodeposited Ni: microstructure and tensile properties, Acta Mater. 50 (2002) 3957–3970, https://doi.org/10.1016/S1359-6454(02)00198-2.

[34] G. Guillonneau, M. Mieszala, J. Wehrs, J. Schwiedrzik, S. Grop, D. Frey, L. Philippe, J.-M. Breguet, J. Michler, J.M. Wheeler, Nanomechanical testing at high strain rates: New instrumentation for nanoindentation and microcompression, Mater. Des. 148 (2018) 39–48, https://doi.org/10.1016/j.matdes.2018.03.050.

[35] L. Hollang, K. Reuther, S.R. Dey, E. Hieckmann, W. Skrotzki, Deformation mechanisms in nanocrystalline nickel at low temperatures, MSF. 683 (2011) 193–201, https://doi.org/10.4028/www.scientific.net/MSF.683.193.

[36] V.V. Shpeizman, V.I. Nikolaev, B.I. Smirnov, V.V. Vetrov, S.A. Pul'nev, V.I. Kopylov, Deformation characteristics of nanocrystalline copper and nickel at low temperatures, Phys. Solid State. 40 (7) (1998) 1151–1154.

[37] Y.M. Wang, E. Ma, On the origin of ultrahigh cryogenic strength of nanocrystalline metals, Appl. Phys. Lett. 85 (2004) 2750–2752, https://doi.org/10.1063/1.1799238.

[38] C. Xiao, R.A. Mirshams, S.H. Whang, W.M. Yin, Tensile behavior and fracture in nickel and carbon doped nanocrystalline nickel, Mater. Sci. Eng.: A 301 (2001) 35–43, https://doi.org/10.1016/S0921-5093(00)01392-7.

[39] Y.J. Li, J. Mueller, H.W. Höppel, M. Göken, W. Blum, Deformation kinetics of nanocrystalline nickel, Acta Mater. 55 (2007) 5708–5717, https://doi.org/10.1016/j.actamat.2007.06.036.

[40] B.E. Schuster, Q. Wei, H. Zhang, K.T. Ramesh, Microcompression of nanocrystalline nickel, Appl. Phys. Lett. 88 (10) (2006) 103112, https://doi.org/10.1063/1.2183814.

[41] J.-A. Lee, B.B. Seo, I.-C. Choi, M.-Y. Seok, Y. Zhao, Z. Jahed, U. Ramamurty, T.Y. Tsui, J. Jang, Time-dependent nanoscale plasticity in nanocrystalline nickel rods and tubes, Scr. Mater. 112 (2016) 79–82, https://doi.org/10.1016/j.scriptamat.2015.09.017.

[42] B. Merle, W.H. Higgins, G.M. Pharr, Extending the range of constant strain rate nanoindentation testing, J. Mater. Res. 35 (2020) 343–352, https://doi.org/10.1557/jmr.2019.408.

[43] J.R. Greer, J.T.M. De Hosson, Plasticity in small-sized metallic systems: Intrinsic versus extrinsic size effect, Prog. Mater Sci. 56 (2011) 654–724, https://doi.org/10.1016/j.pmatsci.2011.01.005.

[44] A. Misra, J.P. Hirth, R.G. Hoagland, Length-scale-dependent deformation mechanisms in incoherent metallic multilayered composites, Acta Mater. 53 (2005) 4817–4824, https://doi.org/10.1016/j.actamat.2005.06.025.

[45] Z. He, F. Wang, Y. Zhu, H. Wu, H.S. Park, Mechanical properties of copper octet-truss nanolattices, J. Mech. Phys. Solids 101 (2017) 133–149, https://doi.org/10.1016/j.jmps.2017.01.019.

[46] K.S. Siow, A.A.O. Tay, P. Oruganti, Mechanical properties of nanocrystalline copper and nickel, Mater. Sci. Technol. 20 (2004) 285–294, https://doi.org/10.1179/026708304225010460.

[47] D. Saraev, R. Miller, Atomic-scale simulations of nanoindentation-induced plasticity in copper crystals with nanometer-sized nickel coatings, Acta Mater. 54 (2006) 33–45, https://doi.org/10.1016/j.actamat.2005.08.030.

[48] R.J. Asaro, S. Suresh, Mechanistic models for the activation volume and rate sensitivity in metals with nanocrystalline grains and nano-scale twins, Acta Mater. 53 (2005) 3369–3382, https://doi.org/10.1016/j.actamat.2005.03.047.

[49] Y.T. Zhu, X.Z. Liao, S.G. Srinivasan, E.J. Lavernia, Nucleation of deformation twins in nanocrystalline face-centered-cubic metals processed by severe plastic deformation, J. Appl. Phys. 98 (2005), https://doi.org/10.1063/1.2006974 034319.

[50] A.L. Patterson, The Scherrer formula for X-Ray particle size determination, Phys. Rev. 56 (1939) 978–982, https://doi.org/10.1103/PhysRev.56.978.

[51] R Development Core Team, R: a language and environment for statistical computing: reference index, R Foundation for Statistical Computing, Vienna, 2010. http://www.polsci.wvu.edu/duval/PS603/Notes/R/fullrefman.pdf (accessed June 21, 2021).

[52] Committee, Practice for determining average grain size using Electron Backscatter Diffraction (EBSD) in fully recrystallized polycrystalline materials, ASTM International, n.d. (2019), https://doi.org/10.1520/E2627-13R19.

[53] F. Ebrahimi, Z. Ahmed, The effect of current density on properties of electrodeposited nanocrystalline nickel, J. Appl. Electrochem. 33 (2003) 733–739, https://doi.org/10.1023/A:1025049802635.

[54] Q. Wei, S. Cheng, K.T. Ramesh, E. Ma, Effect of nanocrystalline and ultrafine grain sizes on the strain rate sensitivity and activation volume: fcc versus bcc metals, Mater. Sci. Eng.: A 381 (2004) 71–79, https://doi.org/10.1016/j.msea.2004.03.064.

[55] J. Lohmiller, M. Grewer, C. Braun, A. Kobler, C. Kübel, K. Schüler, V. Honkimäki, H. Hahn, O. Kraft, R. Birringer, P.A. Gruber, Untangling dislocation and grain boundary mediated plasticity in nanocrystalline nickel, Acta Mater. 65 (2014) 295–307, https://doi.org/10.1016/j.actamat.2013.10.071.

[56] K.S. Kumar, S. Suresh, M.F. Chisholm, J.A. Horton, P. Wang, Deformation of electrodeposited nanocrystalline nickel, Acta Mater. 51 (2003) 387–405, https://doi.org/10.1016/S1359-6454(02)00421-4.
[57] N. Wang, Z. Wang, K.T. Aust, U. Erb, Room temperature creep behavior of nanocrystalline nickel produced by an electrodeposition technique, Mater. Sci. Eng.: A 237 (1997) 150–158, https://doi.org/10.1016/S0921-5093(97)00124-X.
[58] M.J. Kobrinsky, G. Dehm, C.V. Thompson, E. Arzt, Effects of thickness on the characteristic length scale of dislocation plasticity in Ag thin films, Acta Mater. 49 (2001) 3597–3607, https://doi.org/10.1016/S1359-6454(01)00225-7.
[59] M. Legros, B.R. Elliott, M.N. Rittner, J.R. Weertman, K.J. Hemker, Microsample tensile testing of nanocrystalline metals, Philos. Mag. A 80 (2000) 1017–1026, https://doi.org/10.1080/01418610008212096.
[60] C. Peng, Y. Zhong, Y. Lu, S. Narayanan, T. Zhu, J. Lou, Strain rate dependent mechanical properties in single crystal nickel nanowires, Appl. Phys. Lett. 102 (2013), https://doi.org/10.1063/1.4793481 083102.
[61] Y. Wang, A. Hamza, E. Ma, Temperature-dependent strain rate sensitivity and activation volume of nanocrystalline Ni, Acta Mater. 54 (2006) 2715–2726, https://doi.org/10.1016/j.actamat.2006.02.013.
[62] J.F.W. Bishop, A theory of the tensile and compressive textures of face-centred cubic metals, J. Mech. Phys. Solids 3 (1955) 130–142, https://doi.org/10.1016/0022-5096(55)90056-9.
[63] J. Schiøtz, F.D. Di Tolla, K.W. Jacobsen, Softening of nanocrystalline metals at very small grain sizes, Nature 391 (1998) 561–563, https://doi.org/10.1038/35328.
[64] Z. Shan, E.A. Stach, J.M.K. Wiezorek, J.A. Knapp, D.M. Follstaedt, S.X. Mao, Grain boundary-mediated plasticity in nanocrystalline nickel, Science 305 (5684) (2004) 654–657.
[65] X. Wu, Y.T. Zhu, M.W. Chen, E. Ma, Twinning and stacking fault formation during tensile deformation of nanocrystalline Ni, Scr. Mater. 54 (2006) 1685–1690, https://doi.org/10.1016/j.scriptamat.2005.12.045.
[66] R. Niu, X. An, L. Li, Z. Zhang, Y.-W. Mai, X. Liao, Mechanical properties and deformation behaviours of submicron-sized Cu–Al single crystals, Acta Mater. 223 (2022), https://doi.org/10.1016/j.actamat.2021.117460 117460.
[67] S. Ni, Y.B. Wang, X.Z. Liao, H.Q. Li, R.B. Figueiredo, S.P. Ringer, T.G. Langdon, Y.T. Zhu, Effect of grain size on the competition between twinning and detwinning in nanocrystalline metals, Phys. Rev. B. 84 (2011), https://doi.org/10.1103/PhysRevB.84.235401 235401.
[68] J.C.M. Li, Petch relation and grain boundary sources, Transactions of the Metallurgical Society of AIME. 227 (1963) 239–247.
[69] Y.B. Wang, X.Z. Liao, Y.H. Zhao, E.J. Lavernia, S.P. Ringer, Z. Horita, T.G. Langdon, Y.T. Zhu, The role of stacking faults and twin boundaries in grain refinement of a Cu–Zn alloy processed by high-pressure torsion, Mater. Sci. Eng.: A 527 (2010) 4959–4966, https://doi.org/10.1016/j.msea.2010.04.036.
[70] S. Ryu, K. Kang, W. Cai, Predicting the dislocation nucleation rate as a function of temperature and stress, J. Mater. Res. 26 (2011) 2335–2354, https://doi.org/10.1557/jmr.2011.275.
[71] T. Zhu, J. Li, A. Samanta, A. Leach, K. Gall, Temperature and strain-rate dependence of surface dislocation nucleation, Phys. Rev. Lett. 100 (2008), https://doi.org/10.1103/PhysRevLett.100.025502 025502.
[72] R. Ramachandramoorthy, W. Gao, R. Bernal, H. Espinosa, High strain rate tensile testing of silver nanowires: Rate-dependent brittle-to-ductile transition, Nano Lett. 16 (2016) 255–263, https://doi.org/10.1021/acs.nanolett.5b03630.
[73] L. Wang, J. Teng, Y. Wu, X. Sha, S. Xiang, S. Mao, G. Yu, Z. Zhang, J. Zou, X. Han, In situ atomic scale mechanisms of strain-induced twin boundary shear to high angle grain boundary in nanocrystalline Pt, Ultramicroscopy 195 (2018) 69–73, https://doi.org/10.1016/j.ultramic.2018.08.022.
[74] Z.W. Wang, Y.B. Wang, X.Z. Liao, Y.H. Zhao, E.J. Lavernia, Y.T. Zhu, Z. Horita, T.G. Langdon, Influence of stacking fault energy on deformation mechanism and dislocation storage capacity in ultrafine-grained materials, Scr. Mater. 60 (2009) 52–55, https://doi.org/10.1016/j.scriptamat.2008.08.032.
[75] L.F. Hernández Rivera, S. Abolghasem, F.A. Rojas Mora, Mapping the microstructure evolution of nickel deformed by orthogonal cutting, Procedia Manuf. 55 (2021) 238–246, https://doi.org/10.1016/j.promfg.2021.10.034.
[76] A.A. Tiamiyu, E.L. Pang, X. Chen, J.M. LeBeau, K.A. Nelson, C.A. Schuh, Nanotwinning-assisted dynamic recrystallization at high strains and strain rates, Nat. Mater. (2022), https://doi.org/10.1038/s41563-022-01250-0.
[77] J. Panyasantisuk, D.H. Pahr, T. Gross, P.K. Zysset, Comparison of mixed and kinematic uniform boundary conditions in homogenized elasticity of femoral trabecular bone using microfinite element analyses, J. Biomech. Eng. 137 (2015), https://doi.org/10.1115/1.4028968 011002.
[78] M. Holler, A. Diaz, M. Guizar-Sicairos, P. Karvinen, E. Färm, E. Härkönen, M. Ritala, A. Menzel, J. Raabe, O. Bunk, X-ray ptychographic computed tomography at 16 nm isotropic 3D resolution, Sci Rep. 4 (2015) 3857, https://doi.org/10.1038/srep03857.